ISTITUTO NAZIONALE DI RICERCA METROLOGICA
Repository Istituzionale

Printed Zinc Tin Oxide Memristors for Reservoir Computing

Original
Printed Zinc Tin Oxide Memristors for Reservoir Computing / Azevedo Martins, Raquel; Silva, Carlos; Deuermeier, Jonas; Milano, Gianluca; Rosero-realpe, Mateo; Parreira, Carolina; Fortunato, Elvira; Martins, Rodrigo; Kiazadeh, Asal; Carlos, Emanuel. - In: ADVANCED INTELLIGENT SYSTEMS. - ISSN 2640-4567. - 8:1(2026). [10.1002/aisy.202500450]

Availability:
This version is available at: 11696/88381 since: 2026-02-27T08:17:55Z

Publisher:
John Wiley and Sons Inc

Published
DOI:10.1002/aisy.202500450

Terms of use:

This article is made available under terms and conditions as specified in the corresponding bibliographic description in the repository

Publisher copyright

(Article begins on next page)

25 April 2026

Check for updates

RESEARCH ARTICLE

ADVANCED INTELLIGENT SYSTEMS Open Access

www.advintellsyst.com

Printed Zinc Tin Oxide Memristors for Reservoir Computing

Raquel Azevedo Martins, Carlos Silva, Jonas Deuermeier, Gianluca Milano, Mateo Rosero-Realpe, Carolina Parreira, Elvira Fortunato, Rodrigo Martins, Asal Kiazadeh, and Emanuel Carlos**

In this work, fully patterned zinc tin oxide (ZTO) memristors are introduced using inkjet printing. By targeting a scalable, solution-based fabrication approach, highly stable devices with excellent reproducibility and minimal variability are achieved, using ZTO as the active layer, silver (Ag) as the top electrode, and molybdenum as the bottom electrode. The use of sustainable materials like ZTO enhances scalability and environmental compatibility, paving the way for next-generation, low-power neuromorphic computing. The devices successfully fulfill the fundamental criteria for in materia implementation of physical reservoir computing (PRC), including nonlinearity and fading memory property. The devices are successfully trained for classification tasks with MNIST handwritten dataset, achieving 89.4% accuracy and 86.5% by processing 4-bit and 5-bit input temporal sequences. The integration of printed memristors into hardware-based PRC architecture simplifies training complexity, making them particularly advantageous for energy-efficient, wearable AI systems.

1. Introduction

The development of new technologies and the amount of data generated in the last few years have brought an exponential increment in electronic devices and wearables production and consumption.[1] The current silicon technology cannot fulfill the requirements of the present-day internet of things (IoT), as it is reaching its limitations in terms of power consumption and miniaturization.[2] So, it is crucial to have other technologies emerging such as printed electronics.

Printing brings new ways to manufacture electronic devices by combining new materials and deposition techniques. It allows high-volume production of thin and flexible materials at low-cost with less energy consumption since it does not need vacuum methods or a high temperature environment.[3,4] Consequently, it reduces production cost, and it allows the use of greener materials contributing to a more sustainable economy.[5] However, ink optimization, substrate compatibility, and alignment of multilayers with high-resolution are still the main challenges of this technology.[6]

One of the most promising devices in electronics is the memristor, since it allows numerous approaches to overcome the von Neumann approach.

Integrating printing techniques into hardware could enhance the compatibility of physical reservoir computing (PRC) systems, enabling scalable, low-cost, and flexible implementations. To fabricate printed memristors, it is required to choose a printing technique that allows for both good resolution and the formation of films with low surface roughness, as memristors require smooth thin films to reach higher yields and better electrical performance. Inkjet printing is one of the most reported methods for printing memristors.[4] It is a widely used technique classified into continuous inkjet (CIJ) and drop-on-demand (DoD) systems. In DoD printing, the positioning of the droplet on the substrate depends on the relative motion between the drop and the substrate, the timing of the ejection, and the number of nozzles selected from the printhead array. The droplet generation is enhanced by the deformation of a piezoelectric material when applied to an electrical signal. Thus, the droplets of ink are ejected.[7] This method enables high-resolution patterning without the use of masks, eliminating the need for additional patterning steps, and it is compatible with both flexible and rigid substrates.[8] Also, the versatility of this method extends to a broad range of ink formulations, including metals, polymers, and oxides, given that they meet the fluid requirements needed for this method.[9] Beyond research applications, inkjet printing has proven its value in industrial production, supporting the scalable manufacturing of electronic devices and other functional materials.[10,11] For printed memristors, there are several

---

R. Azevedo Martins, C. Silva, J. Deuermeier, C. Parreira, E. Fortunato, R. Martins, A. Kiazadeh, E. Carlos
CENIMAT/i3N Departamento de Ciência dos Materiais
NOVA School of Sciences and Technology (NOVA FCT)
Universidade NOVA de Lisboa
CEMOP/UNINOVA
Caparica 2829-516, Portugal
E-mail: a.kiazadeh@fct.unl.pt; e.carlos@fct.unl.pt

G. Milano
Advanced Materials Metrology and Life Science Division
INRiM
Strada delle Cacce, 91, Torino 10135, Italy

M. Rosero-Realpe
Department of Applied Science and Technology
Politecnico di Torino
Corso Duca degli Abruzzi, 24, Torino 10129, Italy

The ORCID identification number(s) for the author(s) of this article can be found under https://doi.org/10.1002/aisy.202500450.

© 2025 The Author(s). Advanced Intelligent Systems published by Wiley-VCH GmbH. This is an open access article under the terms of the Creative Commons Attribution License, which permits use, distribution and reproduction in any medium, provided the original work is properly cited.

DOI: 10.1002/aisy.202500450

materials that can be used as resistive switching layers such as, 0D quantum dots,[12] 2D materials,[13] nanowires,[14] organic materials,[15] and metal oxides.[16,17] From these, zinc tin oxide (ZTO) is a promising amorphous metal oxide semiconductor (AOS) for printed memristor applications, offering a combination of environmental sustainability, cost-effectiveness, and versatility.[18] Synthesized through solution-based methods, ZTO allows for tunable stoichiometry and can be processed at relatively low temperatures. Unlike indium gallium zinc oxide (IGZO), ZTO avoids the use of indium and gallium, critical and costly elements, thereby enhancing its environmental and economic appeal.[19]

Most reported literature on solution-processed ZTO memristors is based on nanostructures using spin coating as a deposition method,[18–20] while other studies leverage aluminum-doped films to enhance the performance[21–25] (more on Table S1, Supporting Information). The inherent characteristics of ZTO, including its amorphous nature, nontoxic composition, and compatibility with inkjet printing, position it as a sustainable and efficient material for neuromorphic computing devices.[22] State-of-the-art of solution-processed ZTO memristors mostly target nonvolatile applications, whereas these devices operating in the volatile regime can also be exploited as building blocks for the implementation of reservoir systems. This area has been gaining significant attention as an efficient and sustainable alternative to traditional deep learning approaches.[26] Its core concept lies in utilizing the intrinsic dynamics of a reservoir, usually a complex nonlinear dynamical system, to transform input data into a high-dimensional feature space.[27] Recently, this has been applied in materia implementation in memristive devices and systems of the PRC paradigm, a type of brain-inspired computing that excels at processing time-dependent data.[11,28,29]

Unlike conventional neural networks, only the readout layer of PRC requires training, while the reservoir itself remains untrained, reducing computational overhead and energy demands.[26] Memristor-based reservoirs have emerged as promising candidates for hardware implementation of PRC due to their inherent nonlinear dynamics, short and long-term memory properties, and energy efficiency.[29,30] These devices enable compact and scalable architectures while taking advantage of their physical properties to replicate the temporal and spatial dynamics necessary for processing time-series data, making them well-suited for real-time applications such as signal processing and edge computing.[1]

In this work, we report fully patterned ZTO memristors with printed active and top layers, fabricated with different areas, which underwent testing for their potential in PRC applications. Using ZTO as printed active layer and Ag as top electrode, it was possible to produce stable devices with high reproducibility and low variability. Due to its volatile nature, criteria for reservoir computing were demonstrated. It was possible to program the memristor with the MNIST handwritten dataset by processing a 4-bit temporal and 5-bit temporal sequences with an accuracy of 89.4% and 86.5%, respectively.

2. Results and Discussion

Fully patterned devices are fabricated with several areas, 500 × 500, 300 × 300, and 100 × 100 μm^2, where the bottom electrode is sputtered molybdenum (Mo), the active layer and top electrode are ZTO, and silver ink (Ag) printed by piezoelectric inkjet, respectively.

2.1. ZTO Precursor Solution Characterization

Figure 1a presents the thermogravimetry (TG) and differential scanning calorimetry (DSC) of the ZTO precursor solution with a concentration of 0.4 M. Prior to analysis, the precursor solution was stirred at 100 °C for 8 h to evaporate the majority of the solvent. The DSC results reveal a single exothermic peak at 143 °C, accompanied by a significant mass loss of 50%. This behavior indicates the formation of ZTO through a sol–gel synthesis process using 2-methoxyethanol (2-ME) as the solvent. Notably, 2-ME acts both as a solvent and a fuel, facilitating the oxidation of zinc and tin at relatively low temperatures without the need for an additional fuel source.[31] However, 5% v/v of ethylene glycol (EG) was added to the solution to increase the viscosity and improve the homogeneity of the solution.[32] The ink viscosity was measured to examine if it could be printed by an inkjet that requires low viscosity ranges (1–30 cP). An average viscosity of [3.34 ± 0.22] cP was achieved which was compatible with inkjet printing. Moreover, to guarantee a uniform printability, the inverse Ohnesorge (Z) number must be in a specific range ($1 < Z < 10$).[33] In this case, ZTO precursor ink had a Z value of 9.64 (Table S2, Supporting Information), being inside the required range.

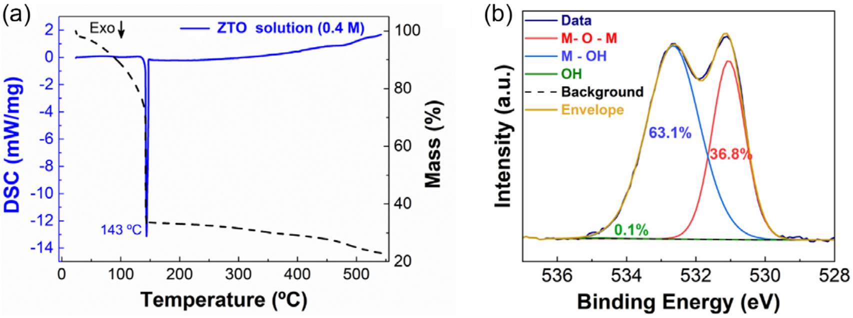

Figure 1. a) DSC-TG of the ZTO precursor solution (0.4 M) using 2-ME as solvent and b) O 1s emission of ZTO printed film annealed at 250 °C.

© 2025 The Author(s). Advanced Intelligent Systems published by Wiley-VCH GmbH

26404567, 2026, 1, Downloaded from https://advanced.onlinelibrary.wiley.com/doi/10.1002/aisy.202500450 by Gianluca Milano - Politecnico Di Torino Sist. Bibl Del Polit Di Torino , Wiley Online Library on [27/02/2026]. See the Terms and Conditions (https://onlinelibrary.wiley.com/terms-and-conditions) on Wiley Online Library for rules of use; OA articles are governed by the applicable Creative Commons License

2.2. ZTO Thin Film and Device Morphology

Figure S1, Supporting Information illustrates the morphological analysis of the inkjet-printed ZTO films on Corning glass substrates. A 1 × 1 mm square was printed at varying resolutions, that are quantified as drops per inch (dpi), to optimize the ink deposition parameters since it directly impacts the electrical behavior of the final devices. Before printing, 15 min UV treatment was performed to improve the wettability and better adhesion of the ink.[34] Despite the prevalence of the coffee ring effect, which is a common issue in printing,[35] the film printed at 1270 dpi exhibited better uniformity and spread characteristics compared to the others. Figure 1b shows the ZTO film O 1s spectra from X-ray photoelectron spectroscopy (XPS). The spectrum demonstrates three peaks at 531.1, 532.6, and 534.8 eV. The first two peaks, *M*-*O*-M and *M*-OH are related to lattice oxygen and nonlattice oxygen. The third peak is attributed to hydroxyl groups that influence the content of oxygen vacancies that affect the transport properties and consequently, the performance of resistive switching devices.[36,37]

The memristors were fabricated with varying device areas and subsequently subjected to electrical characterization to evaluate their performance. For each device area, 18 memristors were produced and tested. **Figure 2**a–c displays optical microscope images of the fabricated devices, that reveal a successful fabrication process, with the devices fully patterned and two-thirds of the structure produced via printing techniques. Detailed topographical characterization of the memristors presented in Figure 2a–c is provided in Figure S2 Supporting Information through profilometry 3D mapping measures. The analysis revealed that all samples exhibit low surface roughness, however, the printed layers display artifacts commonly associated with solution-processed thin films.[4]

2.3. Fully Patterned ZTO Memristors: Electrical Characterization

The pristine states of the memristors were obtained in the voltage range of –0.5 to 0.5 V, with a current compliance of 1 mA to prevent breakdown. The corresponding pristine I–V curves are available in Figure S3, Supporting Information. Different pristine resistivity values are observed for different areas. Larger areas are more prone to exhibiting lower resistivity, and some also show resistive switching characteristics, while smaller ones tend to exhibit more resistive pristine states. This difference is likely due to the printing and annealing processes of the Ag electrode, which may have contributed to an increase in device resistivity.[33]

Endurance tests for 100 cycles were conducted to evaluate the performance and reliability of the devices. Figure 2d–f illustrates the I–V curves of the memristors with varying sizes, which exhibit bipolar resistive switching behavior. The devices demonstrate an abrupt SET at positive voltage ($V_{\mathrm{SET}} \approx 0.8$ V) and a gradual RESET with negative voltage ($V_{\mathrm{RESET}} \approx -0.5$ V). Furthermore, the endurance tests confirm stable performances at low operating voltage, with low variability observed in both the SET and RESET processes across all functional devices.

Device-to-device variation was analyzed, as detailed in Figure S4, Supporting Information, that presents one cycle of each working device across the different areas studied and their SET and RESET variation. Concerning memristors' reproducibility, devices with 300 × 300 μm^2 have the highest yield (83%), followed by 500 × 500 μm^2 with a yield of 77%. Memristors with the smaller area reveal the lower yield (33%), as predicted by the resistive pristine I–V curves. Although 500 × 500 μm^2 devices achieved higher ON/OFF current ratio, the 300 × 300 μm^2 devices have superior performance and have smaller areas. Thus, subsequent electrical characterization was focused exclusively on memristors with a 300 × 300 μm^2 area.

To evaluate the volatility of the devices, retention tests were performed, as presented in Figure S5, Supporting

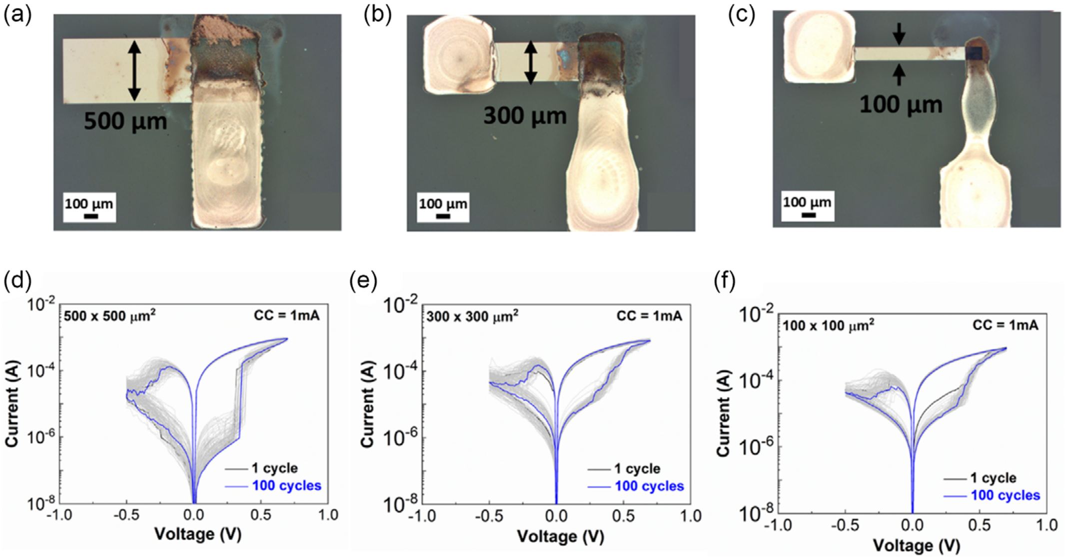

Figure 2. Microscope images of fully patterned Mo/ZTO/Ag devices with different areas: a) 500 × 500 μm^2, b) 300 × 300 μm^2, c) 100 × 100 μm^2; respective I–V sweep for 100 cycles of each device, d) 500 × 500 μm^2, e) 300 × 300 μm^2, and f) 100 × 100 μm^2.

© 2025 The Author(s). Advanced Intelligent Systems published by Wiley-VCH GmbH

26404567, 2026, 1, Downloaded from https://advanced.onlinelibrary.wiley.com/doi/10.1002/aisy.202500450 by Gianluca Milano - Politecnico Di Torino Sist. Bibl Del Polit Di Torino , Wiley Online Library on [27/02/2026]. See the Terms and Conditions (https://onlinelibrary.wiley.com/terms-and-conditions) on Wiley Online Library for rules of use; OA articles are governed by the applicable Creative Commons License

Information. The test illustrates the retention behavior of the device presented in Figure 2e up to 10^4 s. The device initially demonstrates nonvolatile behavior, maintaining an ON/OFF ratio of 10^2 until it drops almost to the OFF-state current, indicating its volatile nature. Volatility is a critical characteristic of memristors, as it is the parameter that determines their potential application for storage (in case of long-term memory) or for processing information over time (in case of short-term memory).[30]

Similar characteristics of volatile ZTO memristors have been reported before using the spin coating technique to deposit ZTO with n^+ Si substrate and indium as electrodes.[21] In these devices, the conductive filaments form and break through the oxygen vacancies present in the ZTO layer. However, when silver is used as an electrode, an additional mechanism comes into play. Upon applying voltage, an electric field is generated, causing Ag^+ ions to migrate through the ZTO layer due to the electrochemical activity of Ag^+.[37] Once the electric field is removed, a spontaneous dissolution of the filament occurs, leading the rupture of the formed filaments.

2.4. Physical Reservoir Computing (PRC) and Bit-Cell Programming

There are specific characteristics of memristors that need to be considered to optimize their performance for the PRC concept. One of them can be assessed by analyzing the device's paired-pulse facilitation (PPF) properties that evaluate the adaptive response of our PRC devices when stimulated by temporally correlated voltage pulses. In this test, two sequential pulses are applied to the device with 0.1 V of amplitude and 100 ns width, varying the time between each pulse, with the response after the second pulse being measured to assess any enhancement relative to the first. The PPF in the memristor is calculated by Equation (1)

$$\text{PPF Index} = \frac{(A_2 - A_1)}{A_1} \tag{1}$$

In which A_1 and A_2 are the currents after the first and second pulse, respectively. The exponential relation between the PPF index and the pulse intervals is presented in **Figure 3**, where the experimental data were fitted with Equation (2)

$$\text{PPF Index} = c_1 e^{-\Delta t/\tau_1} + c_2 e^{-\Delta t/\tau_2} \tag{2}$$

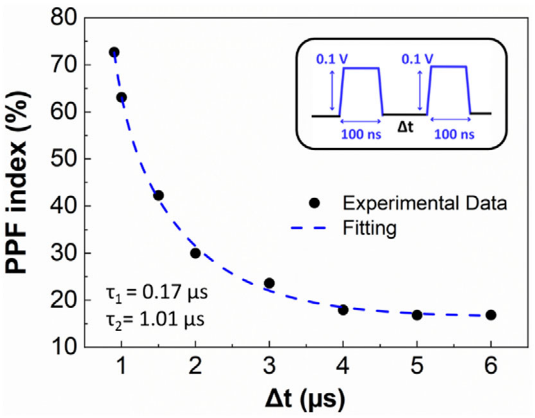

Figure 3. Paired-pulse facilitation (PPF) index for different time intervals.

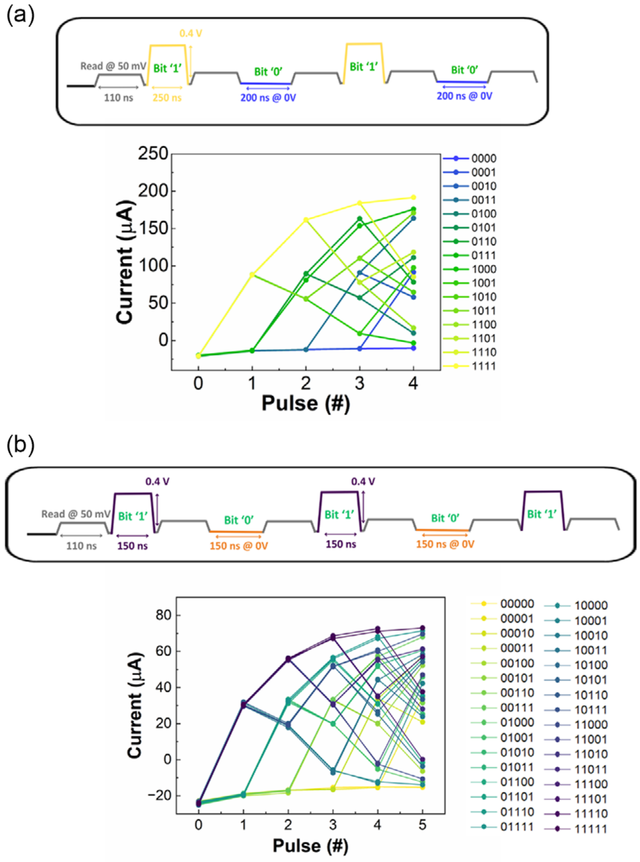

Figure 4. a) Pulse schematic used for 4-bit sequence: bit '1' corresponds to a pulse with 250 ns and 0.4 V and bit '0' corresponds to a 0 V pulse with 200 ns width (mean of 100 cycles) and b) pulse schematic used for 5-bit sequence: bit '1' corresponds to a pulse with 150 ns and 0.4 V and bit '0' corresponds to a 0 V pulse with 150 ns width (mean of ten cycles).

where c_1 and c_2 are the magnitudes of the pulses and τ_1 and τ_2 are the characteristic relaxation times of the respective stages. If the memristor remembers the first pulse and responds more strongly to the second one, this is called facilitation. In this case, this facilitation effect indicates that the device retains a temporary memory of the first pulse for 0.17 μs, with a degree of facilitation on the second pulse when the time interval used is short, as observed in Figure 3. Such behavior is essential in PRC, where a memory of recent past inputs allows the system to process temporal data efficiently, making PPF a valuable tool in optimizing memristors for tasks involving sequential and time-dependent information. Another characteristic is the study of the "fading memory effect" of the device related to the short-term memory of the internal resistance state of the system. This was tested by evaluating the device response to single voltage pulses, varying its amplitude and width. Results reported in Figure S6, Supporting Information show that higher amplitudes and wider pulses lead to higher device current responses, which

© 2025 The Author(s). Advanced Intelligent Systems published by Wiley-VCH GmbH

26404567, 2026, 1, Downloaded from https://advanced.onlinelibrary.wiley.com/doi/10.1002/aisy.202500450 by Gianluca Milano - Politecnico Di Torino Sist. Bibl Del Polit Di Torino , Wiley Online Library on [27/02/2026]. See the Terms and Conditions (https://onlinelibrary.wiley.com/terms-and-conditions) on Wiley Online Library for rules of use; OA articles are governed by the applicable Creative Commons License

proportionally increases the time required for the device to restore the initial (ground) state (relaxation time). Figure S7, Supporting Information presents the time constant (τ) calculations for different pulses applied and the time constant of the device. Although the device operates mainly in the resistive switching regime, short electrical pulses can lead to a dominant capacitive response, with the capacitance depending on the current resistance state. Nevertheless, these capacitive effects do not impair the proper functioning of the PRC system, since the device still processes the temporal-dependent input signals.

Another key performance is the separation property in physical RC, which in the here reported implementation, refers to the ability of the system to distinguish between different input pulse sequences. In these tests, the separation property was evaluated by examining pulse sequence responses taking cycle-to-cycle (c2c) variation into consideration, as shown in **Figure 4**a with mean values of 100 cycles. Each cycle sequence is presented in Figure S8, Supporting Information. This test confirms that the system can reliably separate to different input patterns while maintaining consistent responses across cycles, which is essential for high-performance PRCs. In these terms, the final state of the device endows information of the specific input sequence applied to the device in the recent past.

Typically, PRC approach is performed using 4-bit pulse sequences mainly because the higher the number of bits on the programming sequence, the harder it becomes to differentiate between each one of the current levels associated with each sequence.[29,38,39]

Here, the potential performance impact of using 5-bit sequences on the PRC system was also evaluated. Figure 4b shows the mean values of device separation capabilities using 5-bit programming sequences. The same characteristics for ten cycles are shown in the figure presented in supporting information, Figure S9 Supporting Information.

2.5. MNIST Handwritten Dataset Implementation

In order to validate the effectiveness of the device in terms of information processing capabilities, we benchmarked its performance in the MNIST handwritten digit classification task.[40] The readout currents shown in Figure 4a can be interpreted as the reservoir's response to different combinations of purple and yellow pixels. In this case, purple pixels correspond to a write pulse (0.4 V, 250 ns), while yellow pixels are represented by the absence of a pulse (0 V, 150 ns). As depicted in **Figure 5**a, the digits used for training and testing were first cropped into 28 × 28 pixel images, with the resulting image being binarized. Afterwards, the 784 pixels were grouped into 4-pixel sequences, resulting in a total of 196 4-bit sequences that completely describe the digit intended for classification, where each bit sequence represents a temporal sequence applied to a memristive cell. In our experiment, each of the 4-bit sequences obtained from one device is randomly associated with the current level response, as shown in Figure 5b. This procedure is carried out using the full set of 60 000 handwritten digits from the MNIST training dataset,

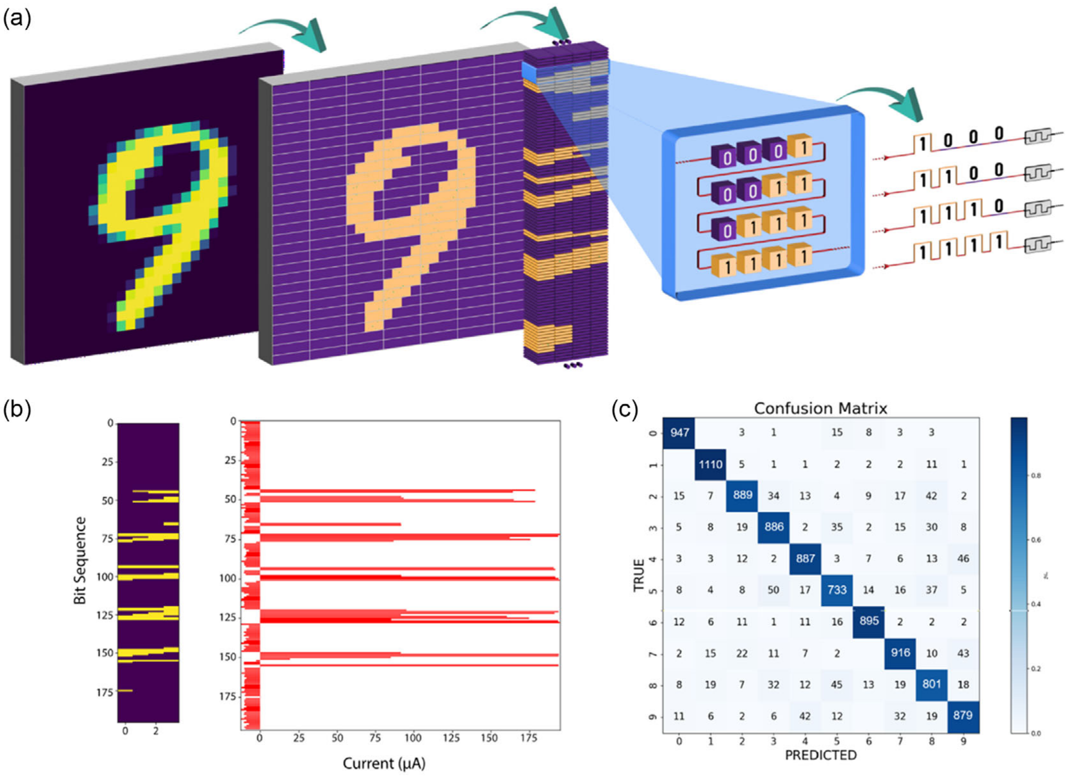

Figure 5. MNIST handwriting digits dataset: a) image of digit 9 with 28 × 28 pixels followed by the binarization of the image with the same pixels size where those pixels are grouped into 4-bit sequences for classification; b) corresponding currents for each bit sequence that are classified as '0' or '1'; and c) matrix obtained from the training with the prediction of the bits accuracy.

© 2025 The Author(s). Advanced Intelligent Systems published by Wiley-VCH GmbH

26404567, 2026, 1, Downloaded from https://advanced.onlinelibrary.wiley.com/doi/10.1002/aisy.202500450 by Gianluca Milano - Politecnico Di Torino Sist. Bibl Del Polit Di Torino , Wiley Online Library on [27/02/2026]. See the Terms and Conditions (https://onlinelibrary.wiley.com/terms-and-conditions) on Wiley Online Library for rules of use; OA articles are governed by the applicable Creative Commons License

followed by an evaluation of its inference performance over 10 000 digits. The classification is done using a simple linear classifier comprised of only two layers, a 196-node input layer and a 10-node output layer (for the 4-bit configuration). For this process, a categorical cross-entropy loss function was chosen, and the accuracy of the network was optimized through a stochastic gradient descent algorithm with adaptive learning rates. Following training, the network achieved an accuracy of 89.4% on the MNIST test dataset. Most of the errors occurred when the model confused the digit "5" with "3" or mistook "8" for "5", as illustrated in Figure 5c.

Building on these results, we retested them using the previously employed MNIST benchmark, now adapted for 5-bit sequences, achieving a classification accuracy of 86.5%. This resulted in only a slight accuracy reduction of 2.9%, while significantly decreasing the overall training parameters by 28%. This approach enables us to test key aspects of the model and impact of number of bits, while evaluating computational efficiency and accuracy. This reduction in training parameters not only leads to an overall simpler PRC system but also more energy efficient due to the reduction in required computational operations.

3. Conclusion

In this study, we successfully fabricated fully patterned solution-based ZTO memristors. The fabrication processes and materials used cost-effective solution-based and printing techniques. Also, the use of sustainable materials like ZTO enhances the environmental friendliness and long-term viability of such systems.

The memristors presented good endurance and stability, with low device-to-device variation showing a yield of 83% for devices with 300 × 300 μm^2. We demonstrate the capability of these devices for the physical reservoir computing concept. Implementing reservoir computing directly in hardware simplifies the design and reduces the complexity of training, making it particularly beneficial for wearable applications. The memristor with the best reproducibility was used to study the characteristics needed for PRC programming. The MNIST handwriting dataset was used to program the memristor and a 4-bit temporal sequence was successfully programmed with 100 cycles endurance with an accuracy of 89.4%. The same scheme was tested using 5-bit temporal sequences, showing an accuracy of 86.5% and reducing the training parameters by 28%. These results highlight the great potential of solution-based ZTO memristors for integration into 4-bit and 5-bit reservoir computing physical systems, a breakthrough for printing memristor applications.

4. Experimental Section

Precursor Solution Synthesis and Characterization: The metallic precursor solutions were prepared by dissolving individually zinc nitrate hexahydrate ($Zn(NO_3)_2 \cdot 6H_2O$, Thermo Scientific Chemicals, 98%) and tin chloride ($SnCl_2 \cdot 2H_2O$, Sigma, 98%) in 2-Methoxyethanol (2-ME, $C_3H_8O_2$, Sigma-Aldrich, 99.8%), to produce solutions with a concentration of 0.4 M. In order to accelerate the process, ammonium nitrate (NH_4NO_3, Roth, 98%) was added to the zinc solution in 1:(1/3) proportion instead of the tin oxide solution. Individual solutions were magnetically stirred between each step for a few minutes. Then, the zinc oxide and tin oxide precursor solutions were mixed with a zinc proportion of 75% and 5% v/v of EG (CH_2OHCH_2OH, Carlo Erba, 99.5%) was added to the precursor solution and afterwards stirred for 24 h at 430 rpm. The precursor solution was prepared in an air ambient environment at room temperature. The solution was filtered with a PTFE 45 μm filter and 1.5 mL of the solution was loaded in a Samba cartridge.

TG-DSC (Netzsch, TG-DSC-STA 449 F3 Jupiter) was performed to the ZTO precursor solution under air atmosphere up to 550 °C with a 10 °C min^{-1} heating rate in an aluminum crucible. The viscosity of the ink was measured to obtain the Z parameter with a CAP 2000+ Viscometer (Brookfield), using a Brookfield Cap 01 spindle and a 67 μl sample with 400 rpm at 30 °C.

Thin Film Deposition and Device Fabrication: Prior to device fabrication, Corning glass substrates (2.5 × 2.5 cm) were subsequently cleaned in an ultrasonic bath of acetone and isopropanol, followed by rinsing with deionized water and dried with a nitrogen spray gun.

For the bottom electrode, a 60 nm thick molybdenum layer was deposited by radio-frequency (RF) magnetron sputtering in an AJA-1800 system with a flow rate of 50 sccm of argon, sputtering power of 175 W, and a deposition pressure of 1.7 mTorr. Bottom electrode patterning was done by reactive ion etching in a Trion Phantom 3 system, using SF6 with areas of 1500 × 500, 1000 × 300, and 1000 × 100 μm^2.

Previous active layer printing, a 15 min UV/ozone treatment was done on the patterned Mo bottom electrodes. The active layer was printed using ZTO precursor ink and a Dimatix DMP-2850 dpi inkjet system printer (Fujifilm) with Samba cartridges of 2.4 pL droplet volume. The ZTO thin film was printed at 1270 dpi with two nozzles at 30 °C with a printing frequency of 5 kHz. The ZTO was printed with areas of 700 × 700, 500 × 500, and 300 × 300 μm^2 followed by a two-step annealing: first at 130 °C for 10 min followed by 250 °C for 30 min.

As top contact, silver nanoparticle ink (Ag Nanoink IJ36, XTPL) was printed using a Dimatix 10 pL cartridge (DMCLCP-16 110) with a printing frequency of 5 kHz. The printer stage and cartridge were set at 50 and 35 °C, respectively. One layer was printed on top of the ZTO with two nozzles with areas of 500 × 1500, 300 × 1000, and 100 × 1000 μm^2. The printed films were dried at 130 °C for 10 min followed by an annealing at 250 °C for 40 min. During the printing process, the temperature and relative humidity were approx. 18–20 °C and 70%, respectively.

Thin Film and Device Characterization: The printing resolution of the active and top layers was characterized using optical microscopy (Zeiss Axiscope 5). The surface of the samples was analyzed using a Bruker DektakXT profilometer in 3D mapping mode. The scan was conducted with a resolution of 3 μm. XPS was measured with a Kratos Axis Supra spectrometer. A monochromatic Al Kα source was used and for the detailed scans, the analyzer was set to pass an energy of 20 eV. Ultraviolet photoelectron spectroscopy (UPS) was performed with the same instrument using He I radiation from a gas discharge lamp. The data was analyzed with CasaXPS software. The quasistatic current–voltage (I—V) characteristics and the pulse studies of the devices were measured using a Keithley 4200 SCS semiconductor analyzer connected to a Janis ST-500 probe station. The bias was applied to the top electrode, maintaining the bottom electrode connected to the ground. The speed of the measurements was set to normal mode, and the integration time was in auto setting. The relaxation properties of the devices were measured using the setup described previously, with the addition of a waveform generator (Keysight 33500B Series) connected to the Janis ST-500 probe station that applied input pulses. The MNIST dataset base was used to program the data. The training data used was randomly picked from a pool of values obtained during endurance cycling tests of 4-bit or 5-bit sequences on the device.

Supporting Information

Supporting Information is available from the Wiley Online Library or from the author.

© 2025 The Author(s). Advanced Intelligent Systems published by Wiley-VCH GmbH

26404567, 2026, 1, Downloaded from https://advanced.onlinelibrary.wiley.com/doi/10.1002/aisy.202500450 by Gianluca Milano - Politecnico Di Torino Sist. Bibl Del Polit Di Torino , Wiley Online Library on [27/02/2026]. See the Terms and Conditions (https://onlinelibrary.wiley.com/terms-and-conditions) on Wiley Online Library for rules of use; OA articles are governed by the applicable Creative Commons License

Acknowledgements

This work was financed by national funds from FCT-Fundação para a Ciência e a Tecnologia, I.P., in the scope of the projects LA/P/0037/2020, UIDP/50025/2020, and UIDB/50025/2020 of the Associate Laboratory Institute of Nanostructures, Nanomodelling and Nanofabrication–i3N. R.A.M. and C.S. thank the Fundação para a Ciência e Tecnologia (FCT) for financial support under the Ph.D. grants (2022.13773.BD and 2021.07840.BD). E.C., A.K., and J.D. acknowledge funding received from FCT via 2021.03825.CEECIND, 2021.03386.CEECIND, and CEECINST/00102/2018, respectively. The authors acknowledge the FCT for funding received with project OPERA via 2022.08132.PTDC and project VOCMemsense via DRI/India/0430/2020. The authors further acknowledge the TERRAMETA project no. 10109710. This work also received funding from the HORIZON-EIC-2023-PATHFINDERCHALLENGES-01 program, grant agreement no. 101161114 (ELEGANCE).

G.M. acknowledges the support of the European Research Council (ERC) under the European Union's ERC Staring grant (ERC-2024-STG) agreement "MEMBRAIN" no. 101 160 604.

Conflict of Interest

The authors declare no conflict of interest.

Author Contributions

The sample fabrication and characterization were performed by **Raquel Azevedo Martins** and **Carlos Silva**. The manuscript was prepared by **Raquel Azevedo Martins** and **Carlos Silva**. All authors examined, commented, and have given approval to the final version of the manuscript. **Raquel Azevedo Martins** and **Carlos Silva** contributed equally to this work.

Data Availability Statement

The data that support the findings of this study are available from the corresponding author upon reasonable request.

Keywords

fully patterned, memristor, physical reservoir computing, printed memristors, solution-based, ZTO

Received: April 22, 2025
Revised: June 26, 2025
Published online: August 3, 2025

[1] R. Wang, J. Yang, S. Han, et al., *Adv. Intell. Syst.* **2020**, *2*, 2000055.
[2] C. A. MacK, *IEEE Trans. Semicond. Manuf.* **2011**, *24*, 202.
[3] M. Berggren, D. T. Simon, H. Hentzell, et al., *Adv. Mater.* **2016**, *28*, 1911.
[4] M. Franco, A. Kiazadeh, R. Martins, S. Lanceros-Méndez, and E. Carlos, *Adv. Electron. Mater.* **2024**, *10*, 2400212.
[5] H. Li, S. Wang, X. Wu, et al., *Nano Energy* **2022**, *101*, 107585.
[6] E. Carlos, R. Branquinho, R. Martins, A. Kiazadeh, and E. Fortunato, *Adv. Mater.* **2021**, *33*, 2004328.
[7] B. Derby, *Annu. Rev. Mater. Res.* **2010**, *40*, 395.
[8] Y. Liu, F. Fischer, J. Aghassi-Hagmann, et al., *Adv. Funct. Mater.* **2024**, *35*, 2412372.
[9] C. Tong, Advanced Materials for Printed Flexible Electronics **2022**, *317*, 53.
[10] Y. Khan, A. Thielens, S. Muin, J. Ting, C. Baumbauer, and A. C. Arias, *Adv. Mater.* **2020**, *32*, 1905279.
[11] M. Pereira, J. Deuermeier, A. Kiazadeh, et al., *Adv. Electron. Mater.* **2020**, *6*, 2000242.
[12] G. W. Baek, Y. J. Kim, J. Kwak, et al., *Nano Lett.* **2024**, *24*, 5855.
[13] M. Delfag, R. Katoch, J. Jehn, Y. Gonzalez, C. Schindler, and A. Ruediger, *Flex. Print. Electron.* **2021**, *6*, 035011.
[14] Z. Cui, Y. Han, Q. Huang, J. Dong, and Y. Zhu, *Nanoscale* **2018**, *10*, 6806.
[15] J. Jehn, M. Kaiser, U. Moosheimer, A. Ruediger, and C. Schindler, *Microelectron. Eng.* **2021**, *239–240*, 111524.
[16] M. Franco, A. Kiazadeh, J. Deuermeier, S. Lanceros-Méndez, R. Martins, and E. Carlos, *Sci. Rep.* **2024**, *14*, 1.
[17] J. Chen, Q. Xu, M. Wang, et al., *IEEE Electron Device Lett.* **2024**, *45*, 1076.
[18] C. Silva, J. Deuermeier, A. Kiazadeh, et al., *Adv. Electron. Mater.* **2023**, *9*, 2300286.
[19] C. Silva, J. Martins, A. Kiazadeh, et al., *Electron. Mater.* **2021**, *2*, 105.
[20] J. Chen, S. Jia, Y. Li, et al., *Colloids Surf., A* **2024**, *689*, 133673.
[21] C. C. Hsu, Y. T. Chen, P. Y. Chuang, and Y. S. Lin, *IEEE Trans. Electron Devices* **2018**, *65*, 2812.
[22] S. Murali, J. S. Rajachidambaram, S. Y. Han, C. H. Chang, G. S. Herman, and J. F. Conley, *Solid State Electron* **2013**, *79*, 248.
[23] T. W. Kim, I. J. Baek, and W. J. Cho, *Solid State Electron* **2018**, *140*, 122.
[24] C. C. Hsu, Y. T. Chen, and C. C. Tsao, *J. Alloys Compd.* **2017**, *696*, 697.
[25] T.-W. Kim, and W.-J. Cho, *J. Nanosci. Nanotechnol.* **2019**, *19*, 6099.
[26] G. Tanaka, T. Yamane, A. Hirose, et al., *Neural Networks* **2019**, *115*, 100.
[27] M. Cucchi, S. Abreu, G. Ciccone, D. Brunner, and H. Kleemann, *Neuromorph. Comput. Eng.* **2022**, *2*, 032002.
[28] G. Milano, G. Pedretti, C. Ricciardi, et al., *Nat. Mater.* **2021**, *21*, 195.
[29] R. Midya, Z. Wang, J. J. Yang, et al., *Adv. Intell. Syst.* **2019**, *1*, 1900084.
[30] K. Nakajima, *Jpn. J. Appl. Phys.* **2020**, *59*, 060501.
[31] D. Salgueiro, A. Kiazadeh, E. Fortunato, et al., *J. Phys. D Appl. Phys.* **2017**, *50*, 065106.
[32] E. Carlos, R. Martins, E. Fortunato, R. Branquinho, *Chem. Eur. J.* **2020**, *26*, 9099.
[33] L. Nayak, S. Mohanty, S. K. Nayak, and A. Ramadoss, *J. Mater. Chem. C* **2019**, *7*, 8771.
[34] E. Carlos, R. Branquinho, R. Martins, A. Kiazadeh, and E. Fortunato, *Adv. Mater.* **2020**, *2004328*, 1.
[35] Y. Li, L. Lan, J. Peng, et al., *ACS Appl. Mater. Interfaces* **2017**, *9*, 8194.
[36] M. S. Rajachidambaram, A. Pandey, S. Vilayurganapathy, P. Nachimuthu, S. Thevuthasan, and G. S. Herman, *Appl. Phys. Lett.* **2013**, *103*, 171602.
[37] R. Waser, R. Dittmann, C. Staikov, and K. Szot, *Adv. Mater.* **2009**, *21*, 2632.
[38] D. Ju, and S. Kim, *Chin. J. Phys.* **2024**, *91*, 361.
[39] H. Ryu, and S. Kim, *Chaos, Solitons Fractals* **2021**, *150*, 111223.
[40] Y. LeCun, L. Bottou, Y. Bengio, and P. Haffner, *Proc. IEEE* **1998**, *86*, 2278.

© 2025 The Author(s). Advanced Intelligent Systems published by Wiley-VCH GmbH

26404567, 2026, 1, Downloaded from https://advanced.onlinelibrary.wiley.com/doi/10.1002/aisy.202500450 by Gianluca Milano - Politecnico Di Torino Sist. Bibl Del Polit Di Torino , Wiley Online Library on [27/02/2026]. See the Terms and Conditions (https://onlinelibrary.wiley.com/terms-and-conditions) on Wiley Online Library for rules of use; OA articles are governed by the applicable Creative Commons License